Available online at www.sciencedirect.com

jmr&t Journal of Materials Research and Technology

journal homepage: www.elsevier.com/locate/jmrt

Original Article

First-principles calculations to investigate HgY_2S/Se_4 spinel chalcogenides for optoelectronic and thermoelectric applications

Ghulam M. Mustafa [a,*], Sadaf Saba [b], N.A. Noor [c], A. Laref [d], Magda Abd El-Rahman [e,f], Zahid Farooq [a], R.B. Behram [g], Zaka Ullah [a]

[a] Department of Physics, Division of Science and Technology, University of Education, Lahore, Punjab 54770, Pakistan

[b] Computational Materials Modeling Laboratory, Department of Physics, Government College University, Faisalabad, 38040, Pakistan

[c] Department of Physics, RIPHAH International University, Campus Lahore, Pakistan

[d] Department of Physics and Astronomy, College of Science, King Saud University, Riyadh, 11451, Saudi Arabia

[e] Department of Physics, College of Science, King Khalid University, Abha, 61413, Saudi Arabia

[f] Department of Radiation Physics, National Center of Radiation Research and Technology (NCRRT), Atomic Energy Authority, 11787Cairo, Egypt

[g] Department of Physics, AIOU, Islamabad, Pakistan

ARTICLE INFO

Article history:
Received 15 September 2022
Accepted 19 November 2022
Available online 25 November 2022

Keywords:
HgY_2S/Se_4 spinels
Ab-initio calculations
Direct small bandgap semiconductors
Optical characteristics
Thermoelectric efficiency

ABSTRACT

Spinel chalcogenides have great potential for optoelectronic and thermoelectric applications and therefore received huge attention in recent years. In this regard, here we investigate the structural, optical, electronic, and thermoelectric characteristics of HgY_2S_4 and HgY_2Se_4 spinel chalcogens using a density functional theory-based WIEN2k package. Ground state optimization of crystal structure and thermodynamic stability of the material is probed from the energy volume optimization graph and computation of enthalpy of formation. The computation of Poisson's and Pugh's ratios revealed the ductile nature of these materials. Bandgap calculation is performed using TB-mBJ package, which exposed the direct band nature of these semiconducting materials with bandgap values of 1.2 eV for HgY_2S_4 and 0.6 eV for HgY_2Se_4. The evaluation of optical characteristics and transport features revealed these compositions' potential for optoelectronic and thermoelectric applications.

* Corresponding author.
E-mail address: dr.ghulam.muhammad@ue.edu.pk (G.M. Mustafa).

https://doi.org/10.1016/j.jmrt.2022.11.119

1. Introduction

Thermoelectric materials are the potential alternatives for harvesting devices like thermoelectric generators whose efficiency is measured in the form of the figure of merit (ZT). This figure of merit depends upon the Seebeck coefficient (S), electrical conductivity (σ), and thermal conductivity (κ). The value of ZT can be calculated using the expression $ZT = S^2\sigma T/\kappa$ [1] where the term $S^2\sigma$ is called the power factor (PF) and determines the efficiency of thermoelectric materials without considering the effect of thermal conductivity [2]. The material with a high value of PF is usually heavily doped semiconductors like Bi_2Te_3. In semiconductors, the thermal conductivity mainly comes from the lattice thermal conductivity governed by phonons [3]. For better performance of any thermoelectric material it must have higher values of S, σ, and PF with minimal κ [4]. Thermoelectric materials with a small thermal conductivity value are highly desirable for advanced technological applications [5]. In this paper, we evaluated the spinel structured material with the general formula AM_2X_4 where A is divalent, M is a trivalent atom, and X is a chalcogen atom. Atom A occupies 1/8th of the tetrahedral positions, and atom M occupies half of the octahedral positions, whereas X atoms form the FCC lattice [6]. Spinel compositions cover a broad spectrum of applications because of the significant mixing of cations at A and M sites ranging from optical to electronic, magnetic to optoelectronic, and medical to industrial. For their potential applicability in thermoelectric applications, Spitzer proposed that the high coordination number of M atoms favors reducing the thermal conductivity of spinels [7]. High concentrations of octahedral holes present in the lattice act as a scattering center for phonons and thus reduce thermal conductivity. Therefore, this kind of composition with a multi-valley electronic structure is supposed to reveal a high value of power factor [8].

Spinel chalcogenides have been extensively studied compositions in the last few decades. More than 300 known spinel compositions are reported with X = S or Se in which most have 3d transition metals at M and A-sites [9]. In addition to spinel chalcogenides, oxides-based spinel compositions have also been explored to evaluate their magnetic response, but they are not feasible for thermoelectric devices because of their very high bandgap values [6]. Furthermore, the sulfides-based compositions are usually conductors or small band semiconductors, for example, sulfides of Fe, Ni, Co, and V are not stable in spinel and transform to M_3S_4 type under high pressure and temperature. The spinels with X = Te are conductors with a small value of power factor. Spinel selenides are exceptional thermoelectric materials because of their low thermal conductivity and their wide spectrum of electronic properties ranging from metals to insulators [10]. Therefore, optimizing doping concentration to obtain minimal thermal power is desirable but challenging for *p* and *n*-type semiconductors [11]. The Skutterudites and Zn_4Sb_3 are proven thermoelectric materials but could not accommodate a variety of dopants to obtain minimum thermal conductivity. Thanks to the chemical versatility of $A_xM_{3-x}X_4$ compositions, these compositions can accommodate a variety of dopants which allows tuning the thermal conductivity and other thermoelectric properties [12]. Spinel chalcogenides are promising materials and get huge attention because of their broad spectrum applications in thermoelectric devices [13]. Here, we evaluated the structural, optical, electronic, and thermoelectric characteristics of HgY_2S_4 and HgY_2Se_4 compounds by first-principles calculations. Because, Y-based spinel chalcogenides have been studied as cost-effective magnetic materials, so they have great potential for spintronic applications like quantum computing, quantum valve, and magnetic memory devices [14]. The presence of Y in the spinel lattice provides a conducting channel for Hg ions and make them good for low-temperature catalytic property [15]. In addition to spinels, a detailed investigation of electronic, optical, mechanical, and thermodynamic studies of full, half, and quaternary Heusler alloys [16–21]. On the other hand, double perovskite materials have also been extensively explored for their optoelectronic and thermoelectric application for futuristic devices [22–27].

However, a limited number of investigations are available to understand the mercury adsorption and oxidation method of S and Se-based chalcogenides. Since there are no theoretical or experimental reports in the literature available for thermoelectric investigations of Y-based spinels HgY_2S/Se_4, and here we first time explored the optical, electronic, and thermoelectric properties of these materials to check their potential for optoelectronic and thermoelectric applications. The higher values of the figure of merit (ZT) and the computed small bandgap indicate that Y-based spinels HgY_2S/Se_4 are suitable for energy conversion applications.

2. Computational analysis

The optoelectronic and thermoelectric poperties of Y-based spinels HgY_2S/Se_4 were computed within the framework of the WIEN2k code [28–33], based on density functional theory. We employed the generalized gradient approximation (GGA) proposed by Perdew, Burke, and Ernzerhof (PBE) for the electronic exchange-correlation energy functional. The potentials were created by considering the outermost electrons of an atom and give accurate results of structure parameters comparable to experiment. For exchange-correlation energy functional, local density approximation (LDA) is also used, but it give results underestimate as compared to GGA. We did modified Becke-Johnson (mBJ) potential calculations by considering electronic and optical properties and found that mBJ potential slightly increase the bandgap [34–40]. Furthermore, modified Becke-Johnson potential (mBJ) has been employed for calculating the bandgap close to the actual band bap of the material because this code generates more reliable bandgap values [41]. A variarty of approxinmations have been utilized to compute different physical features of these materials [42–50]. The ground state structural parameters are calculated by relaxing and optimizing the unit cell which leads to estimate the electrical and optical characteristics of the HgY_2S/Se_4. In the interstitial region, the cut-off parameter of the plane ave function was set. The order of k-mesh was 10 × 10 × 10, which generated 1000 k-points. On the other hand, the values of R_{MT} x K_{max} and G_{max} were kept at 8 and 16, respectively where R_{MT} represent the radius of smalles unit

cell in reciprocal space called the muffin tin radius and K_{max} denoted the maximum value of K-vector. The energy was converged as 10^{-5} Ry. Afterward, using the BoltzTrap code [51], the thermoelectric parameters of HgY_2S/Se_4 spinels were investigated.

3. Results and discussion

3.1. Structural parameters

Fig. 1 presents the crystallographic arrangement of HgY_2S/Se_4 spinels in stick and ball format and then in a polyhedral form. The blue-colored cations are of Hg placed at the tetrahedral site, black-colored cations are of Y placed at the octahedral site, and yellow-colored anions are of S/Se developing FCC lattices [52].

Before calculating any physical property, the structure was first relaxed in its ground state to determine the ground state lattice parameters. The fitting of structural data with the Birch-Murnaghan equation of state generated the value of ground state optimized volume of unit cell which is used to compute the lattice constant a_o(Å) and Bulk modulus B_o(GPa). The computed values of a_o and B_o are presentd in Table 1. It can be noticed from these values that the value of a_o enhanced while the value of B_o reduced by keeping S at Se place. This variation in a_o and B_o is caused by the higher ionic radius of Se rather than S. The thermodynamic stability is further verified by measuring the enthalpy of formation (ΔHf).

$$\Delta H_f = E_{total}\left(Hg_lY_mS/Se_n\right) - lE_{Hg} - mE_Y - nE_{S/Se} \quad (1)$$

E_{total} (Hg_lY_mS/Se_n) is the overall energy, whereas E_{Hg}, E_Y, and $E_{S/Se}$ are the energies of Hg, Y, and S/Se, respectively. HgY_2S/Se_4 spinels are thermodynamically stable because the measured values of ΔH_f have negative energy values.

The mechanical response of HgY_2S/Se_4 spinels was estimated by computing three elastic constants i.e., C11, C12, and C44 which pave the path to calculate various moduli of elasticity. These elastic constants help to define the stability criteria for cubic systems (C11 > 0, C11 + 2C12 > 0, and C11−C12 > 0) called the Born stability criteria. The computed values of these constants also support the stability of these compositions. Using the calculated values of elastic constant, we calculate bulk modulus (B), Young modulus (Y), and Shear modulus (S), and their estimated values are given in Table 1. The measured values of bulk modulus B_o (GPa) from elastic parameters and computed from structural optimization data represent that studied spinels reveal better mechanical properties. To identify whether the material is uctile or brittle, the Pugh ratio (B/G) and Poisson ratio (υ) play their key role becaue if the value of B/G is ≥ 1.75 the maerial is ductile other wise brittle similarly the if the value of υ ≥ 0.26 the material is ductile other brittle. In present scenario, the value of B/G is 1.75 and 1.78 where as value of υ is 0.26 and 0.27 for HgY_2S_4 and HgY_2Se_4 respectively which assured their ductile nature [53].

Fig. 2(a) and (b) present the volume energy optimization graphs for HgY_2S_4 and HgY_2Se_4. The value of the optimized

Table 1 – Computed structural and elastic parameters of HgY_2S_4 and HgY_2Se_4 spinels.

Parameters	HgY_2S_4	HgY_2Se_4
	PBEsol-GGA	PBEsol-GGA
a_o(Å)	11.12	11.62
B_o (GPa)	76.19	63.65
ΔH_f	−8.64	−6.88
C_{11}	150.23	112.40
C_{12}	39.84	32.68
C_{44}	37.45	29.85
B	73.63	59.25
G	42.05	33.49
Y	110.29	84.56
B/G	1.75	1.77
υ	0.26	0.27
A	0.68	0.75

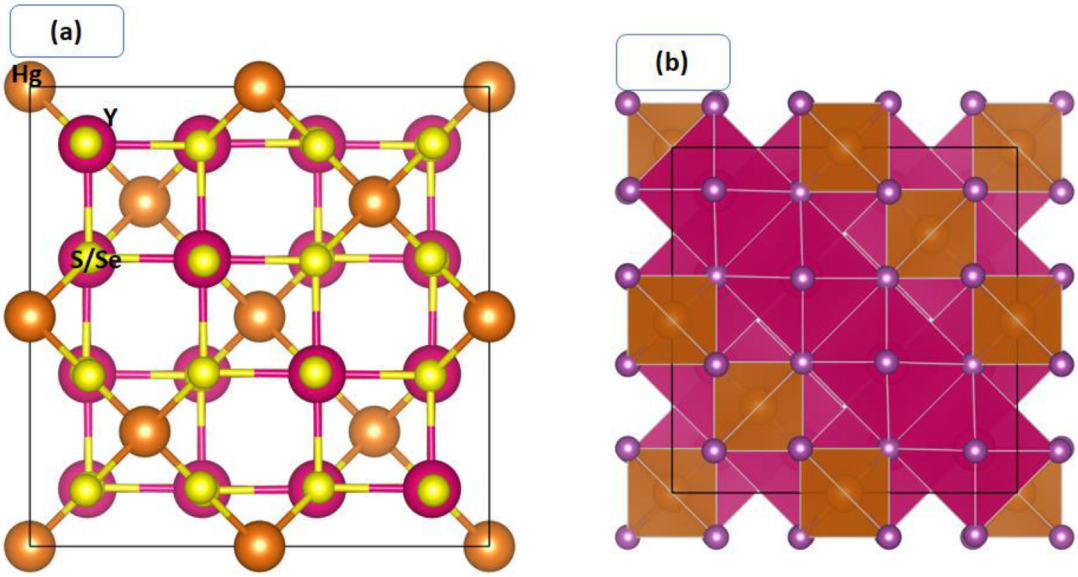

Fig. 1 – Unit cell of HgY_2S/Se_4 in (a) ball-stick model and (b) polyhedral format.

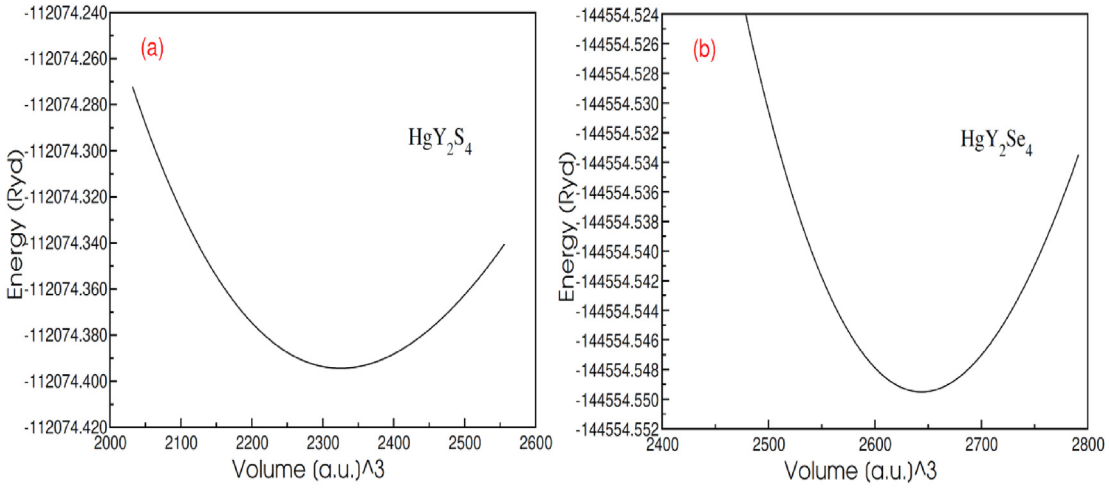

Fig. 2 – Energy-volume optimization graph of HgY_2S_4 and HgY_2Se_4 spinels.

lattice constant is determined from the lowest point on this curve. By keeping S at Se place, the lowest point appeared at a relatively higher volume value, indicating the unit cell's expansion. The larger ionic radii of Se, contrary to the S expanded the unit cell.

3.2. *Electronic band structure*

The band structure analysis aims to understand the material's nature and appropriateness in device fabrications. The band structure of HgY_2S/Se_4 spinels is observed in Fig. 3. Both compositions possess direct band gap structure and small bandgap values for both compositions reveal their semiconducting nature. The computed bandgap (E_g) value for HgY_2S_4 is found to be 1.2 eV which is reduced to 0.6 eV when S is replaced with Se. The higher atomic radii of Se caused this reduction in Eg value compared to S atoms [54–56]. These narrow bandgap semiconductors are appropriate for optoelectronic devices working in the infrared region of the electromagnetic spectrum.

Interband jumping probability of electrons is governed by density of states and band strucutre. This is because the hybridization of involving states plays a decisive role in defining the bandgap and, thus, the electronic transition. To have a deep look of involving states of contributing atoms in band formation, the graphs of total density of states (TDOS) and partial density of states (PDOS) are presented in Fig. 4. A closer look at the PDOS revealed that 5*d*-states of Hg, 4*s*-states of Y and 3*p*-states of S and Se form the valence band in which 5*d*-states of Hg are deep in the valence band, appeared around −5.5 eV for HgY_2S_4, and move further down to −6 eV for HgY_2Se_4. However, 4*s*-states of Y spread between −3.5 and −0.5 eV. However, the valence band edge is formed by the 3*p*-states of S and Se, which touches the Fermi level. The conduction band is composed of 4*s*-states of Y and 3*p* states of S and Se. When Se replaces S, 4*s* states of Y and 3*p* states of Se in

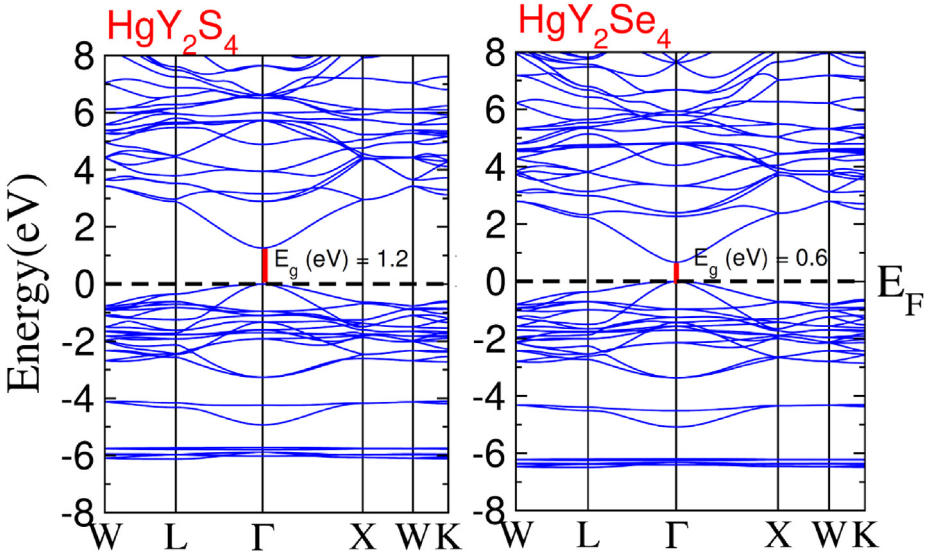

Fig. 3 – Band structure of HgY_2S_4 and HgY_2Se_4compositions.

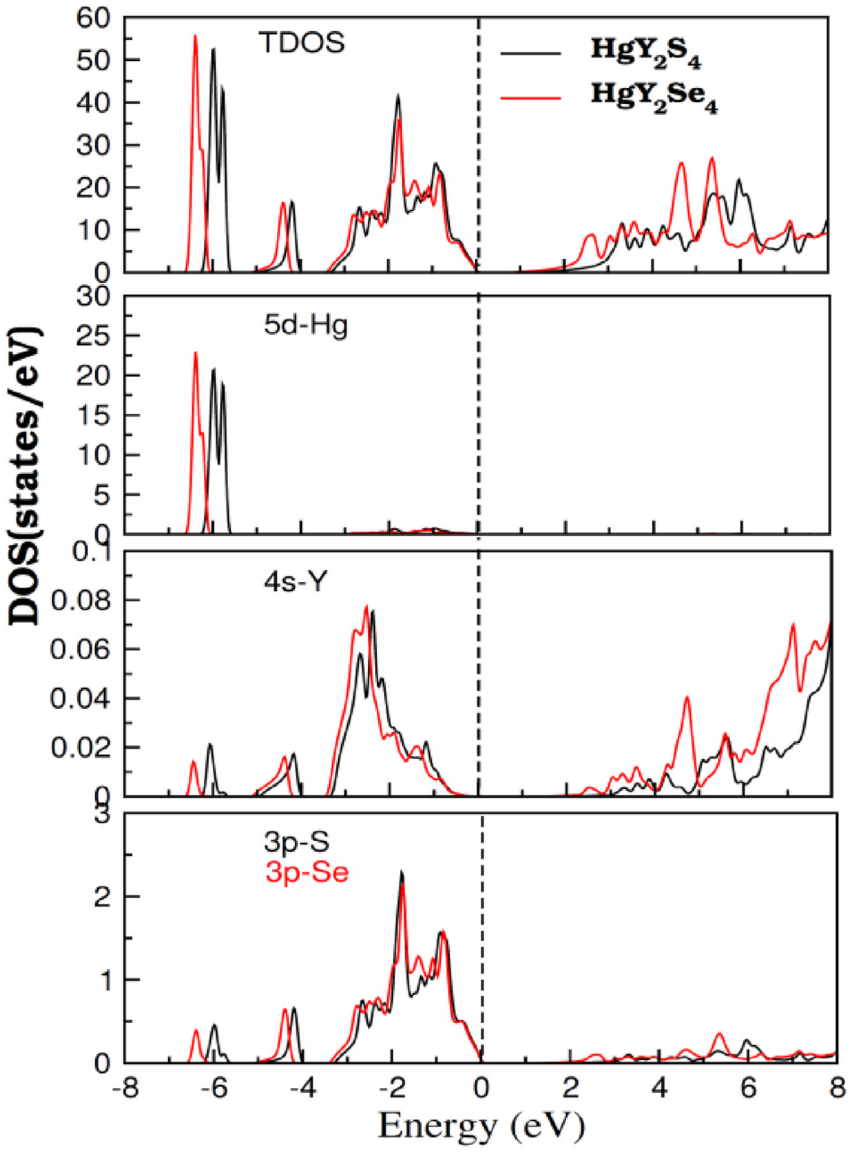

Fig. 4 – Total and partial density of states for HgY_2S_4 and HgY_2Se_4 spinels.

the CB moved towards the fermi level, which caused the net reduction in the E_g value from 1.2 to 0.6 eV. This replacement is a powerful approach to tuning the spinel chalcogenides bandgap, making them suitable for optoelectronic and thermoelectric devices [57,58].

3.3. *Optical characteristics*

The calculated values of band gap energy (E_g) and static dielectric constant $\varepsilon_1(0)$ are given in Table 2 for HgY_2S_4 and HgY_2Se_4 compositions along with refractive index (n(0)) and reflectivity (R(0)) values. It is observed that values of $\varepsilon_1(0)$, n(0), and R(0) are increased by replacing S atoms with Se. The Se atoms have higher atomic radii, so their density is high that's why the refractive index is high. Similarly, its polarizability is higher than HgY_2S_4 composition; therefore, it shows a higher value of $\varepsilon_1(0)$ [59].

Table 2 – Energy bandgap E_g(eV), real part of dielectric constant $\varepsilon_1(0)$, refractive index n(0) and reflectivity R(0) at 0 energy for HgY_2S_4 and HgY_2Se_4.

Parameters	HgY_2S_4	HgY_2Se_4
	Our work	
E_g(eV)	1.20	0.60
$\varepsilon_1(0)$	5.89	7.09
n(0)	2.42	2.66
R(0)	0.17	0.21

The dielectric constant is a complex quantity $\varepsilon(\omega) = \varepsilon_1(\omega) + i\varepsilon_2(\omega)$, whose real $\varepsilon_1(\omega)$ and imaginary $\varepsilon_2(\omega)$ parts were estimated to understand better the optical response of HgY_2S_4 and HgY_2Se_4 spinels [60]. The dispersion and absorption of light can be observed when there is an interaction of photons of light with matter. The former term in $\varepsilon(\omega)$

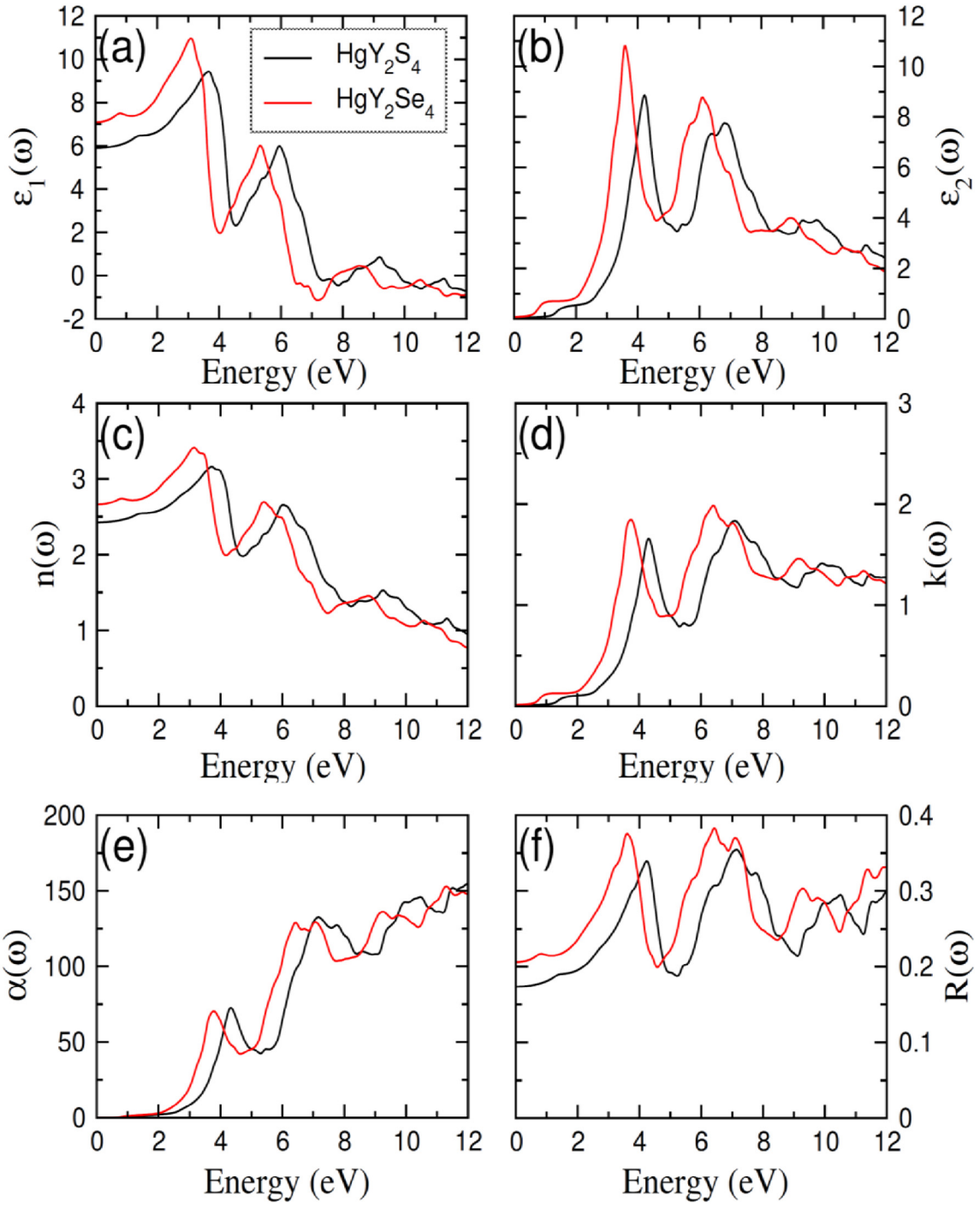

Fig. 5 – Energy dependent (a) $\varepsilon_1(\omega)$, (b) $\varepsilon_2(\omega)$, (c) n(ω), (d) k(ω), (e) α(ω), and (f) R(ω) for HgY_2S_4 and HgY_2Se_4 spinels.

corresponds to the absorption of light, while the latter one corresponds to the dispersion of light. The separate frequency dependent response of real and imaginary part of dielectric conatnt can be understood based on the Kramer-Kroning relation [61]:

In Fig. 5(a–d), the plots of ε_1 (ω), ε_2 (ω), n(ω) and k(ω) are shown where it was noticed that the highest peak of ε_1 (ω) was noticed at 3.8 eV for HgY_2S_4 and 3 eV for HgY_2Se_4. Since the energy and frequency of electromagnetic waves are directly linked, therefore moving of highest intensity peak towards lower energy causes an increase in ε_1 (ω) value from 9 to 11 [62]. In Fig. 5(b), the highest peak of ε_2 (ω) was noticed at 4.1 and 3.8 eV for HgY_2S_4 and HgY_2Se_4, respectively. For the former composition, the value of ε_2 (ω) is zero below 1 eV and subsequent composition this energy limit is 0.6 eV. These spinels are appropriate candidates for optoelectronic

applications in the infrared region. Moreover, ε_1 (ω) is related to the n and k through $n^2 + k^2 = \varepsilon_1$ (ω) relation. The term n(ω) determines how often light slows down in a medium than in a vacuum. The highest inensity peaks for n(ω) and k(ω) are seen at 3.9 eV and 7 eV, respectively for HgY_2S_4 and these peaks are shifted to 3.1 eV and 6.3 eV, for HgY_2Se_4. To further understand the absorption of light, the absorption coefficient α(ω) was calculated and depicted in Fig. 5(e) [63]. In addition, the value of α(ω) quantifies the absorbed light by semiconductors and it became significant when incident light is smaller than bandgap (CB) value. Its value is zero below 2 eV and has maximum peaks at 12 eV for both compositions. It means the studied spinels will absorb more light for higher energies. Absorption, transmission, and reflection all happen concurrently as light strike a surface. Another essential factor for optoelectronic applications, reflectivity R(ω), is shown in Fig. 5(f), which is used to examine the light that is reflected from the surface. In contrast with α(ω), the values of R(ω) are in fractions that's why the performance of optical devices will not be affected [64].

3.4. *Thermoelectric characteristics*

For device applications, it is much needed to measure the thermoelectric factors of the materials because the ability of the device to alter heat into electrical energy can be calculated through these factors [65]. In Fig. 6(a–d), the thermoelectric parameters are plotted in the temperature range of 200–800 K, and their measured readings are given in Table 3.

The moving free carriers correspond to the σ/τ, and its value gradually increased with an increase in temperature for HgY_2S_4 and HgY_2Se_4 spinels [66]. The carriers transition from the valence to the conduction band after getting energy from temperature. The values of σ/τ are lower at lower temperatures and maximum at 800 K temperature for both compositions. Similarly, the heat caused by the carriers and lattice vibrations corresponds to the κ/τ. These lattice vibrations generate the phonon waves. The trend of thermal conductivity concerning temperature is almost similar to that of electrical conductivity, which increases with increasing temperature, but its values are much lower than electrical conductivity [67]. For thermoelectrics, the studied compositions are appropriate candidates owing to their small value of thermal conductivity (10^{14}) and high value of electrical conductivity (10^{19}). The voltage due to the temperature gradient (Seebeck coefficient (S)) is graphed concerning the temperature in Fig. 6(b). The graph shows that the value of S is low for HgY_2S_4 and high for HgY_2Se_4. The positive value of S reveals that these compositions have a p-type semiconducting response [68]. From Fig. 6(d), the plot of the power factor (PF) can be seen through which the thermoelectric efficiency of the material can be found. An increasing trend in PF is noticed for HgY_2S_4 and HgY_2Se_4 spinels against temperature. This factor is calculated to understand the thermoelectric performance of the materials.

The outcome of the combined thermoelectric response is sensed from the figure of merit (ZT). Fig. 7 shows the change of ZT versus temperature, where it increased with growing

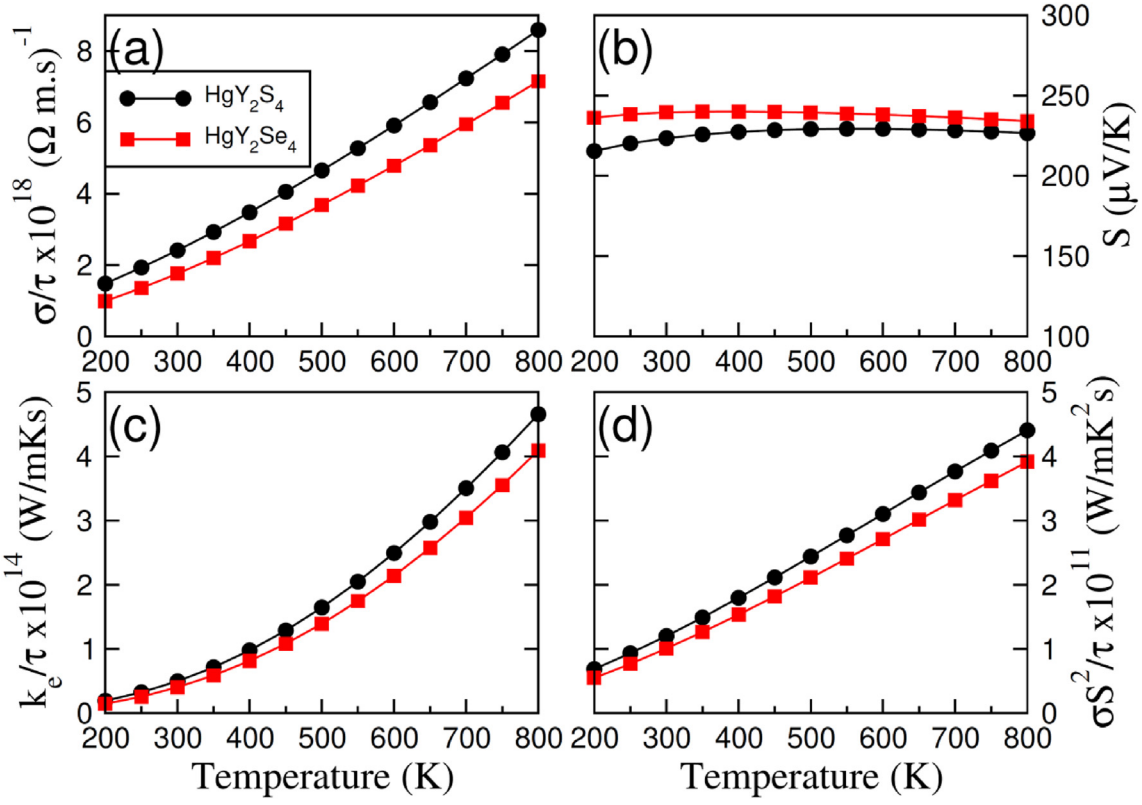

Fig. 6 – Temperature dependent (a)Electrical conductivity (σ/τ), (b)Seebeck coefficient (S),(c) thermal (k_e/τ) conductivity, and (d) power factor ($\sigma S^2/\tau$) of HgY_2S_4 and HgY_2Se_4.

Table 3 – Thermoelectric parameters of HgY_2S_4 and HgY_2Se_4 at RT.

Spinels	σ/τ ($\times 10^{19}$/Ωms)	κ_e/τ ($\times 10^{14}$W/mK)	S(μV/K)	$\sigma S^2/\tau$	ZT
HgY_2S_4	2.41	0.49	223.36	1.20	0.72
HgY_2Se_4	1.76	0.40	239.48	1.01	0.75

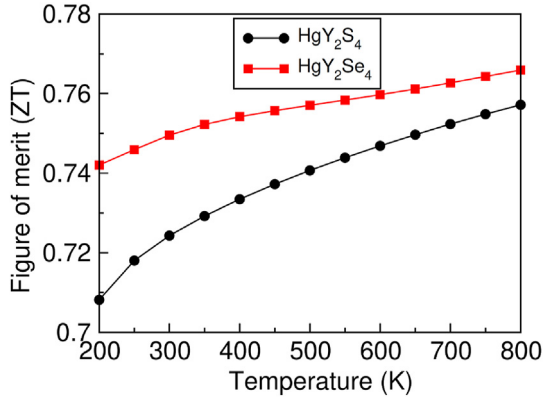

Fig. 7 – Temperature-dependent figure of merit (ZT) of HgY_2S_4 and HgY_2Se_4.

temperature [69]. The value of ZT for HgY_2S_4 is 0.708 and 0.742 for HgY_2Se_4 at 200K. When temperature increases, this value reaches 0.758 for HgY_2S_4 and 0.765 for HgY_2Se_4 at 800K. The higher the ZT values, the more will be the thermal-to-electrical conversion efficiency of the material. These investigations revealed that these compositions are potential materials for high-temperature thermoelectric devices. Comparatively speaking, if a thermoelectric device is fabricated using HgY_2Se_4 material it will reveal better thermoelectric performance even in a higher temperature range i.e., up to 800K.

4. Conclusion

In nut shell, here we theoretically investigated the mechanical, electronic band strucutre and transport properties of HgY_2S/Se_4 by DFT-based software WIEN2k. The ground state stability was probed through formation energy, which manifests that HgY_2S_4 (−8.64 eV) was more stable than HgY_2Se_4 (−6.88 eV). The incorporation of Se at the S site expanded the unit cell and caused an increase in lattice constant from 11.12 to 11.62 Å. In this scenario, the bulk modulus was decreased from 76.19 to 63.65 GPa. Since calculated values of B/G > 1.75 and υ > 0.26, uncovered the ductile nature of these compositions. The small direct bandgap semiconducting nature at Γ- Γ symmetry point is exposed by electronic bandgap analysis. In addition, keeping S at Se place caused the decrease in bandgap value from 1.2 to 0.6 eV, which was suitable for optical devices operating in the infrared region. The computation of thermoelectric properties has been carried out using the BoltzTrap semiclassical approach. The calculation of transport parameters includes the electronic conductivity, thermal conductivity, Seebeck coefficient, power factor, and figure of merit. Based on all these facts, we conclude that the understudy spinel chalcogenides are a potential candidate for thermoelectric applications.

Data availability statement

All data presented in this work can be provided on request.

Declaration of competing interest

The authors declare that they have no known competing financial interests or personal relationships that could have appeared to influence the work reported in this paper.

Acknowledgment

Magda Abd El-Rahman extends their appreciation to the Deanship of Scientific Research at King Khalid University, Abha, Saudi Arabia, for funding this work through Large Groups Project under grant number RGP. 2/73/43.

REFERENCES

[1] Yang L, Huh D, Ning R, Rapp V, Zeng Y, Liu Y, et al. High thermoelectric figure of merit of porous Si nanowires from 300 to 700 K. Nat Commun 2021;12(1):1–7.
[2] Xu T, Haruna AY, Ma Z, Li W, Li J, Luo Y, et al. High power factor and thermoelectric figure of merit in $Sb_2Si_2Te_6$ through synergetic effect of Ca doping. Chem Mater 2021;33(20):8097–105.
[3] Goyal M. Shape, size and phonon scattering effect on the thermal conductivity of nanostructures. Pramana 2018;91(6):1–5.
[4] Xie H, Hao S, Bao J, Slade TJ, Snyder GJ, Wolverton C, et al. All-inorganic halide perovskites as potential thermoelectric materials: dynamic cation off-centering induces ultralow thermal conductivity. J Am Chem Soc 2020;142(20):9553–63.
[5] Pathak R, Sarkar D, Biswas K. Enhanced band convergence and ultra-low thermal conductivity lead to high thermoelectric performance in SnTe. Angew Chem 2021;133(32):17827–33.
[6] Snyder GJ, Caillat T, Fleurial JP. Thermoelectric properties of chalcogenides with the spinel structure. Mater Res Innovat 2001;5(2):67–73.
[7] Spitzer DP. Lattice thermal conductivity of semiconductors: a chemical bond approach. J Phys Chem Solid 1970;31(1):19–40.
[8] Algrafy E, Tariq S, Mahmood Q, Kattan NA, Galani SS, Ramay SM, et al. First principle study of structural, electronic, ferromagnetic, mechanical and thermoelectric properties of ZnMn2X4 (X= S and Se) spinels. Phys Scripta 2020;95(10):105702.
[9] Gupta S. Structural, magnetic and transport properties of some polar intermetallics (stannides and antimonides) and

silver, copper based quaternary thio-spinels. IIT Delhi: Doctoral dissertation; 2007.
[10] Meyer GJ, Biswas K. A special forum issue on thermoelectric energy conversion. ACS Appl Energy Mater 2020;3(3):2037–8.
[11] Cho C, Song Y, Hsu JH, Yu C, Stevens DL, Grunlan JC. Organic thermoelectric thin films with large p-type and n-type power factor. J Mater Sci 2021;56(6):4291–304.
[12] El-Genk MS, Saber HH, Caillat T. Performance tests of skutterudites and segmented thermoelectric converters. AIP Conf Proc, Vol. 699; 2004, February. p. 541–52. 1 American Institute of Physics.
[13] Heiba ZK, Mohamed MB, Badawi A, Farag NM. Effect of sulfur deficiency on the structural, optical and electronic properties of MnS nanostructures. Chem Phys Lett 2021;779:138877.
[14] Robail M, Noor NA, Iqbal MW, Ullah H, Mahmood A, Naeem MA, et al. Comprehensive study of ferromagnetic $MgNd_2X_4$ (X= S, Se) spinels for spintronic and solar cells device applications. Ceram Int 2022;48(2):2385–93.
[15] Batouche M, Belfarh T, Mohammed DES, Tabeti A, Seddi T, Uğur S, et al. External pressure effect on the electronic, optical and thermoelectric properties of the CdY_2Ch_4 (Ch= S, Se) spinel compounds: via modified Becke–Johnson (mBJ) exchange potential. Physica B 2018;545:40–7.
[16] Saim A, Belkharroubi F, Boufadi FZ, Ameri I, Blaha LF, Tebboune A, et al. Investigation of the structural, elastic, electronic, and optical properties of half-heusler CaMgZ (Z= C, Si, Ge, Sn, Pb) compounds. J Electron Mater 2022;51(7):4014–28.
[17] Asma B, Belkharroubi F, Ibrahim A, Lamia B, Mohammed A, Belkilali W, et al. Structural, mechanical, magnetic, electronic, and thermal investigations of Ag2YB (Y= Nd, Sm, Gd) full-Heusler alloys. Emergent Materials 2021;4(6):1769–83.
[18] Belkilali W, Belkharroubi F, Ameri M, Ramdani N, Boudahri F, Khelfaoui F, et al. Theoretical investigations of structural, mechanical, electronic and optical properties of NaScSi alloy. Emergent Materials 2021;4(5):1465–77.
[19] Fadila B, Ameri M, Bensaid D, Noureddine M, Ameri I, Mesbah S, et al. Structural, magnetic, electronic and mechanical properties of full-Heusler alloys Co2YAl (Y= Fe, Ti): first principles calculations with different exchange-correlation potentials. J Magn Magn Mater 2018;448:208–20.
[20] Mentefa A, Boufadi FZ, Ameri M, Gaid F, Bellagoun L, Odeh AA, et al. First-principles calculations to investigate structural, electronic, elastic, magnetic, and thermodynamic properties of full-heusler Rh2MnZ (Z= Zr, Hf). J Supercond Nov Magnetism 2021;34(1):269–83.
[21] Moussali A, Amina MB, Fassi B, Ameri I, Ameri M, Al-Douri Y. First-principles calculations to investigate structural and thermodynamic properties of Ni2Laz (Z= As, Sb and Bi) Heusler alloys. Indian J Phys 2020;94(11):1733–47.
[22] Amin MA, Nazir G, Mahmood Q, Alzahrani J, Kattan NA, Mera A, et al. Study of double perovskites X2InSbO6 (X= Sr, Ba) for renewable energy; alternative of organic-inorganic perovskites. J Mater Res Technol 2022;18:4403–12.
[23] Nazir G, Rehman A, Hussain S, Algrafy E, Mahmood Q, Mera A, et al. Study of narrow band gap double perovskites (Sr/Ba) 2BB'O6 (B= In, Tl, B'= Sb, Bi) for optical, thermoelectric, and mechanical properties. Mater Today Commun 2022;31:103547.
[24] Mahmood Q, Nazir G, Alzahrani J, Kattan NA, Al-Qaisi S, Albalawi H, et al. Room temperature ferromagnetism and thermoelectric behavior of calcium based spinel chalcogenides CaZ2S4 (Z= Ti, V, Cr, Fe) for spintronic applications. J Phys Chem Solid 2022;167:110742.
[25] Albalawi H, Haq BU, Nazir G, Ghrib T, Kattan NA, Mahmood Q, et al. Study of new double perovskite halides Rb2Ti (Cl/Br) 6 for solar cells and thermoelectric applications. Mater Today Commun 2022;32:104106.
[26] Mahmood Q, Nazir G, Rahim A, Alzahrani J, Aljameel AI, Murtaza G, et al. Impact of 5d electrons on half metallic ferromagnetism, and thermoelectric properties of Cs2Z (Cl/Br) 6 (Z= Os, Ir) for spintronic applications. Mater Chem Phys 2022;288:126414.
[27] Ismail K, Murtaza G, Tahir S, Nazir G, Kattan NA, Albalawi H, et al. Theoretical study of electronic, magnetic, optical and thermoelectric properties of XMnO2 (X= Au, Ag, Cu) oxides by DFT. J Solid State Chem 2022;314:123432.
[28] Blaha P, Schwarz K, Madsen GK, Kvasnicka D, Luitz J. WIEN2k. An augmented plane wave+ local orbitals program for calculating crystal properties, 60. Tech Univ Wein; 2001.
[29] Samia L, Belkharroubi F, Ibrahim A, Lamia BF, Saim A, Maizia A, et al. Investigation of structural, elastic, electronic, and magnetic proprieties for X2LuSb (X= Mn and Ir) full-Heusler alloys. Emergent Materials 2022;5(2):537–51.
[30] Radja K, Farah BL, Ibrahim A, Lamia D, Fatima I, Nabil B, et al. Investigation of structural, magneto-electronic, elastic, mechanical and thermoelectric properties of novel lead-free halide double perovskite Cs2AgFeCl6: first-principles calcuations. J Phys Chem Solid 2022:110795.
[31] Zoubir MK, Fadila B, Keltoum B, Ibrahim A, Farah BL, Al-Douri Y, et al. Structural, electronic and thermodynamic investigation of Ag2GdSi, Ag2GdSn and Ag2Gd Pb Heusler alloys: first-principles calculations. Mater Test 2021;63(6):537–42.
[32] Guechi N, Bouhemadou A, Medkour Y, Al-Douri Y, Khenata R, Bin-Omran S. Electronic and thermoelectric properties of the layered Zintl phase CaIn2P2: first-principles calculations. Phil Mag 2020;100(23):3023–39.
[33] Ayad M, Belkharroubi F, Boufadi FZ, Khorsi M, Zoubir MK, Ameri M, et al. First-principles calculations to investigate magnetic and thermodynamic properties of new multifunctional full-Heusler alloy Co2TaGa. Indian J Phys 2020;94(6):767–77.
[34] Perdew JP, Burke K, Ernzerhof M. Generalized gradient approximation made simple. Phys Rev Lett 1996;77(18):3865.
[35] Boudiaf K, Bouhemadou A, Al-Douri Y, Khenata R, Bin-Omran S, Guechi N. Electronic and thermoelectric properties of the layered BaFAgCh (Ch=S, Se and Te): first-principles study. J Alloys Compd 2018;759:32–43.
[36] Bekhti-Siad A, Bettine K, Rai DP, Al-Douri Y, Wang X, Khenata R, et al. Electronic, optical and thermoelectric investigations of Zintl phase AE3AlAs3 (AE= Sr, Ba): first-principles calculations. Chin J Phys 2018;56(3):870–9.
[37] Benkaddour Y, Abdelaoui A, Yakoubi A, Khachai H, Al-Douri Y, Omran SB, et al. First-principle calculations of structural, elastic, and electronic properties of intermetallic rare earth R2Ni2Pb (R= Ho, Lu, and Sm) compounds. J Supercond Nov Magnetism 2018;31(2):395–403.
[38] Yahiaoui IE, Lazreg A, Dridi Z, Al-Douri Y, Bouhafs B. Gd impurities effect on Co2CrSi alloy: first-principle calculations. Bull Mater Sci 2018;41(1):1–5.
[39] Benkabou MH, Harmel M, Haddou A, Yakoubi A, Baki N, Ahmed R, et al. Structural, electronic, optical and thermodynamic investigations of NaXF3 (X= Ca and Sr): first-principles calculations. Chin J Phys 2018;56(1):131–44.
[40] Bidai K, Ameri M, Amel S, Ameri I, Al-Douri Y, Varshney D, et al. First-principles calculations of pressure and temperature dependence of thermodynamic properties of anti-perovskite BiNBa3 compound. Chin J Phys 2017;55(5):2144–55.
[41] Koller D, Tran F, Blaha P. Phys Rev B Condens Matter 2011;83:1–10.
[42] Wen J, Li N, Shi Q, Wu H, Feng X, Wang C, et al. First-principles calculations to investigate electronic structures and magnetic regulation of non-metallic elements doped BP with point defects. J Mol Graph Model 2022:108370.

[43] Asadullayeva SG, Ismayilova NA, Eyyubov QY. Optical and electronic properties of defect chalcopyrite ZnGa2Se4: experimental and theoretical investigations. Solid State Commun 2022;356:114950.
[44] Ameri M, Bennar F, Amel S, Ameri I, Al-Douri Y, Varshney D. Structural, elastic, thermodynamic and electronic properties of LuX (X= N, Bi and Sb) compounds: first principles calculations. Phase Transitions 2016;89(12):1236–52.
[45] Khireddine A, Bouhemadou A, Alnujaim S, Guechi N, Bin-Omran S, Al-Douri Y, et al. First-principles predictions of the structural, electronic, optical and elastic properties of the zintl-phases AE3GaAs3 (AE= Sr, Ba). Solid State Sci 2021;114:106563.
[46] Shafiq S, Hussain A, Rasul MN, Hayat SS, Iqbal F, Rafiq MA. First-principles structural, electronic, optical and bonding properties of scandium-based ternary indide system Sc5T2In4 (T= Ni, Pd, Pt). Bull Mater Sci 2020;43(1):1–10.
[47] Al-Douri Y, Ameri M, Bouhemadou A, Batoo KM. First-principles calculations to investigate the refractive index and optical dielectric constant of Na3SbX4 (X= S, Se) ternary chalcogenides. Phys Status Solidi 2019;256(11):1900131.
[48] Hasni L, Ameri M, Bensaid D, Ameri I, Mesbah S, Al-Douri Y, et al. First-principles calculations of structural, magnetic electronic and optical properties of rare-earth metals TbX (X= N, O, S, Se). J Supercond Nov Magnetism 2017;30(12):3471–9.
[49] Souadia Z, Bouhemadou A, Khenata R, Al-Douri Y. Structural, elastic and lattice dynamical properties of the alkali metal tellurides: first-principles study. Phys B Condens Matter 2017;521:204–14.
[50] Boudiaf K, Bouhemadou A, Boudrifa O, Haddadi K, Saoud FS, Khenata R, et al. Structural, elastic, electronic and optical properties of LaOAgS-type silver fluoride chalcogenides: first-principles study. J Electron Mater 2017;46(7):4539–56.
[51] Madsen GK, BoltzTraP DJ Singh. A code for calculating band-structure dependent quantities. Comput Phys Commun 2006;175:67–71.
[52] Noor NA, Hassan M, Rashid M, Alay-e-Abbas SM, Laref A. Systematic study of elastic, electronic, optical and thermoelectric properties of cubic $BiBO_3$ and $BiAlO_3$ compounds at different pressure by using ab-initio calculations. Mater Res Bull 2018;97:436–43.
[53] Shannon RD. Revised effective ionic radii and systematic studies of interatomic distances in halides and chalcogenides. Acta Crystallogr A 1976;32:751–67.
[54] Jain A, Ong SP, Hautier G, Chen W, Richards WD, Dacek S, et al. Commentary: the Materials Project: a materials genome approach to accelerating materials innovation. Apl Mater 2013;1:011002.
[55] Aguilera I, Palacios P, Sánchez K, Wahnón P. Theoretical optoelectronic analysis of $MgIn_2S_4$ and $CdIn_2S_4$ thiospinels: effect of transition-metal substitution in intermediate-band formation. Phys Rev B 2010;81:075206.
[56] Alay-e-Abbas SM, Javed F, Abbas G, Amin N, Laref A. Density functional theory evaluation of ceramics suitable for hybrid advanced oxidation processes: a case study for Ce^{4+}-doped $BaZrO_3$. J Phys Chem C 2019;123:6044–53.
[57] Liu BW, Zhang MJ, Zhao ZY, Zeng HY, Zheng FK, Guo GC, et al. Synthesis, structure, and optical properties of the quaternary diamond-like compounds I2–II–IV–VI4 (I= Cu; II= Mg; IV= Si, Ge; VI= S, Se). J Solid State Chem 2013;204:251–6.
[58] Wang HC, Pistor P, Marques MA, Botti S. Double perovskites as p-type conducting transparent semiconductors: a high-throughput search. J Mater Chem 2019;7:14705–11.
[59] Zanib M, Noor NA, Iqbal MA, Mahmood I, Mahmood A, Ramay SM, et al. Density functional theory study of electronic, optical and transport properties of magnesium based MgY2Z4 (Z= S and Se) spinels. Curr Appl Phys 2020;20:1097–102.
[60] Penn DR. Wave-number-dependent dielectric function of semiconductors. Phys Rev 1962;128:2093.
[61] Nawaz PA, Mustafa GM, Iqbal SS, Noor NA, Ahmad TS, Mahmood A, et al. Theoretical investigations of optoelectronic and transport properties of Rb2YInX6 (X= Cl, Br, I) double perovskite materials for solar cell applications. Sol Energy 2022;231:586–92.
[62] Iqbal S, Mustafa GM, Asghar M, Noor NA, Iqbal MW, Mahmood A, et al. Tuning the optoelectronic and thermoelectric characteristics of narrow bandgap Rb2AlInX6 (X= Cl, Br, I) double perovskites: a DFT study. Mater Sci Semicond Process 2022;143:106551.
[63] Green MA, Keevers MJ. Optical properties of intrinsic silicon at 300 K. Prog Photovoltaics Res Appl 1995;3:189–92.
[64] Mahmood A, Rashid M, Safder K, Iqbal MW, Noor NA, Ramay SM, et al. Spin-dependent rare-earth-based $MgPr_2X_4$ (X= S, Se) spinels investigations for spintronic and sustainable energy systems applications. Results Phys 2021;20:103709.
[65] Pal K, Anand S, Waghmare UV. Thermoelectric properties of materials with nontrivial electronic topology. J Mater Chem C 2015;3:12130–9.
[66] Mustafa GM, Noor NA, Iqbal MW, Sajjad M, Naeem MA, Mahmood Q, et al. Study of optoelectronic and transport properties of $MgLu_2Z_4$ (Z= S, Se) spinels for optoelectronic and energy harvesting applications. Mater Sci Semicond Process 2021;121:105452.
[67] Khan MA, Alburaih HA, Niaz S, Noor NA, Dahshan A, Yakout HA, et al. Structural, opto-electronic, and transport properties of $HgSc_2S_4$ and $HgSc_2Se_4$ spinel compounds based on density functional theory. Phys Scripta 2021;96:125715.
[68] Mahmood Q, Rashid M, Noor NA, Ashiq MGB, Ramay SM, Mahmood A, et al. Opto-electronic and thermoelectric properties of $MgIn_2X_4$ (X= S, Se) spinels via ab-initio calculations. J Mol Graph Model 2019;88:168–73.
[69] Robail M, Noor NA, Iqbal MW, Ullah H, Mahmood A, Naeem MA, et al. Comprehensive study of ferromagnetic $MgNd_2X_4$ (X= S, Se) spinels for spintronic and solar cells device applications. Ceram Int 2022;48:2385–93.